RSC Advances

PAPER

View Article Online
View Journal | View Issue

Cite this: *RSC Adv.*, 2025, **15**, 25209

Enhanced electrochemical activity of MgO nanoparticles for high-performance supercapacitors†

Megha Goyal,[a] Sarvesh Kumar Pandey *[b] and Nitu Bhatnagar*[a]

To support various forms of energy storage systems for high power requirements, supercapacitors are essential as an additional type of energy storage device. In this study, magnesium oxide nanoparticles (MgONPs) were synthesized using a co-precipitation method and systematically evaluated as active electrode materials. FESEM images revealed a porous and aggregated surface morphology, which may facilitate ion transport by providing accessible diffusion pathways while Raman spectroscopy confirmed the presence of characteristic vibrational modes, including features associated with structural defects, which are commonly observed in nanostructured oxides. The electrochemical behavior of the MgONPs electrode material was evaluated using the three-electrode technique in a 2 M KOH aqueous electrolyte. At a current rate of 1 A g^{-1}, a MgONPs electrode material exhibited a specific capacity of 11 F g^{-1}. The CV behavior demonstrates the strong reversibility of the electrode material revealed a maximum specific capacitance of 99 F g^{-1} at 10 mV s^{-1} and good rate capability, underscoring the potential of MgONPs in energy storage devices. To complement the experimental observations, a density functional theory (DFT) study was conducted to examine the structural stability and electronic properties of MgONPs at the molecular level. The DFT-optimized geometry closely matched experimental lattice parameters, while a low HOMO–LUMO energy gap ($\Delta E = -6.571$ eV) indicated high reactivity and efficient charge transfer. Additional descriptors such as dipole moment, softness, and electrophilicity supported the electrochemical behavior observed experimentally. This integrated computational–experimental approach provides comprehensive insights into the fundamental properties of MgONPs, establishing them as promising, cost-effective, and high-performance electrode materials for next-generation supercapacitor systems.

Received 18th June 2025
Accepted 3rd July 2025

DOI: 10.1039/d5ra04329h

rsc.li/rsc-advances

1. Introduction

The rising demand for electrochemical energy storage (EES) is largely driven by the growing use of renewable energy sources (RES) like solar and wind, and the global push toward cleaner, low-carbon energy solutions.[1,2] Despite advancements, current energy storage systems are insufficient to support large-scale integration of variable energy sources without risking instability in the power grid. In fact, if renewables supply more than 20% of the total energy, the grid could experience serious disruptions.[3,4] Advanced electrochemical storage technologies offer promising solution to address these limitations, enhancing grid reliability, facilitating renewable energy integration, and supporting efficient energy storage and delivery. To meet the rising energy demand, there is a strong focus on developing high-performance energy storage technologies.[5,6]

Among these technologies, supercapacitors (SCs), also known as electrochemical capacitors stand out due to their rapid charging and discharging capabilities, high power output, excellent cycling life, and wide range of applications. SCs find extensive use in electric vehicles, wearable gadgets, and portable electronics.[7–10] They are mainly classified into two types based on their energy storage mechanisms. Electrical double-layer capacitors (EDLCs) store charge through ion adsorption and desorption at the electrode–electrolyte interface, while, pseudocapacitors rely on fast redox (oxidation–reduction) reactions, allowing them to achieve higher capacitance.[11,12] Researchers have explored a variety of active materials for supercapacitor electrodes, including conducting polymers,[13–16] metal oxides, and carbon-based materials.[13,14] Transition metal oxides (TMOs) are particularly notable for their pseudocapacitive behavior.

Kumar *et al.*[17] have reviewed the synthesis methods and applications of nanostructured and microstructured electroactive materials in SCs TMOs such as iron(III) oxide (Fe_2O_3),

[a]*Department of Chemistry, Manipal University Jaipur, Jaipur-303007, Rajasthan, India. E-mail: niturbhatnagar@gmail.com*

[b]*Department of Chemistry, Maulana Azad National Institute of Technology Bhopal, Bhopal-462003, Madhya Pradesh, India. E-mail: sarvesh@manit.ac.in*

† Electronic supplementary information (ESI) available. See DOI: https://doi.org/10.1039/d5ra04329h

niobium pentoxide (Nb_2O_5), zinc oxide (ZnO), nickel oxide (NiO), cobalt oxide (Co_3O_4), cuprous oxide (Cu_2O), molybdenum trioxide (MoO_3), manganese dioxide (MnO_2), and tungsten trioxide (WO_3) have been widely investigated as effective electrode materials.[18–27] Among these, magnesium oxide nanoparticles (MgONPs) have gained attention for applications in sensors, optical devices, and energy storage systems, including batteries and SCs.[28–31] MgO typically crystallizes in a cubic (rock salt) structure under standard conditions. But can exhibit tetragonal, orthorhombic, or hexagonal forms under specific synthesis conditions.[32–34]

Despite its advantages, MgO's low electrical conductivity limits its performance in advanced energy storage systems, especially at high charge–discharge rates.[35] To address this, researchers have developed hybrid electrode materials to enhance electrical conductivity and structural durability. The selection of MgONPs in this current work is further motivated by their qualities, including low production cost, non-toxicity, and environmental friendliness, among others. Various synthesis methods, such as hydrothermal method,[36] sol–gel technique,[37] co-precipitation method,[38] green synthesis method,[39] spray pyrolysis, combustion, and microwave techniques, have been employed to produce MgONPs with diverse morphologies and properties. Factors like concentration, pH, calcination temperature, and ionic strength significantly influence the properties of the synthesized MgONPs[40,41]

Several studies have reported on the energy storage performance of MgONPs and related materials. For instance, a CNT and biomass carbon mixture achieved a specific capacitance of 85 F g^{-1},[42] while rGO/WO_3 composites demonstrated comparable performance.[43] Moreover, the energy storage performance was evaluated using the galvanostatic charge–discharge (GCD) technique. The 120HTMgO-C electrode achieved a specific capacitance of 42 F g^{-1} at a current density of 1 A g^{-1} within a 2.5 V operating window and maintained 93% of its original capacitance after 10 000 charge–discharge cycles.[44] Rostas *et al.* prepared vanadium(v)-doped MgO nanoparticles showed excellent supercapacitor performance, achieving 50 F g^{-1} at 10 mV s^{-1} and 4.17 Wh kg^{-1} energy density. Remarkably, with carbon black, the capacitance surged to 1200 F g^{-1} an unprecedented value for MgO based materials.[45] Table 1 provides a comparative summary of our MgONPs electrode performance with recent literature reports.

In this work, MgONPs were synthesized *via* the co-precipitation method and characterized using various techniques. Electrochemical performance was evaluated in a 2 M KOH electrolyte. A flexible symmetric supercapacitor was fabricated, employing MgONPs as the active material for both electrodes, with carbon black and polyvinylidene fluoride (PVDF) as binder. Electrochemical impedance spectroscopy (EIS) was conducted to assess resistive and capacitive properties at the electrode–electrolyte interface.

The MgONPs electrode, fabricated using an effective sonication process on copper and aluminum foils, exhibited rapid ion diffusion kinetics, enabling high-power output. This study demonstrated the potential of MgONPs as cost-effective, environmentally friendly materials for practical energy storage applications, combining a large surface area and excellent electrical conductivity for efficient ion storage and rapid charge transfer. An *in silico* approach, integrating first-principles density functional theory (DFT) calculations with experimental electrochemical analysis, provided insights into the structural and electronic properties of MgONPs, paving the way for future experimental research.[46–50] This integrated computational-experimental strategy underscores the potential of MgO nanostructures as stable, efficient, and cost-effective electrode materials for high-performance supercapacitor systems.

2. Experimental section

2.1 Materials

Magnesium nitrate hexahydrate ($Mg(NO_3)_2 \cdot 6H_2O$; 98%) were purchased from LOBA Chemie Pvt. Ltd, while potassium hydroxide (KOH, 99%) and PVDF were purchased from HIMEDIA. De-ionized water was used as the solvent throughout the experiments. Carbon black and copper and aluminum foils (purity ≥99%) were used as substrates for electrode fabrication. All chemicals and reagents were used as received without further purification.

2.2 Material characterization

X-ray diffraction (XRD) was utilized to characterize the synthesized MgO nanoparticle electrodes using a Rigaku SMARTLAB diffractometer with Cu Kα radiation ($\lambda = 1.54$ Å). Field emission scanning electron microscopy (FESEM) was performed with a JSM-7610FPlus instrument to examine the surface morphology of the samples. Energy-dispersive X-ray spectroscopy (EDS), conducted using the same JSM-7610FPlus model, was employed to analyze the elemental distribution of metals. The surface functional groups were identified using a Fourier transform infrared (FTIR) spectrophotometer (Bruker Alpha) within the wavenumber range of 4000–500 cm^{-1}. Raman

Table 1 Comparative summary of our MgONPs electrode performance with recent literature reports

Material	Electrolyte	Specific capacitance (F g^{-1})	Current density (A g^{-1})
MgONPs (this work)	2 M KOH	99	0.01
CNT/biomass carbon[42]	2 M KOH	85	1
rGO/WO_3 (ref. 43)	1 M H_2SO_4	85	1
Ni-doped MgO (CTAB)[51]	2 M KOH	96	1
MgO–C (120HT)[44]	Not specified	42	1

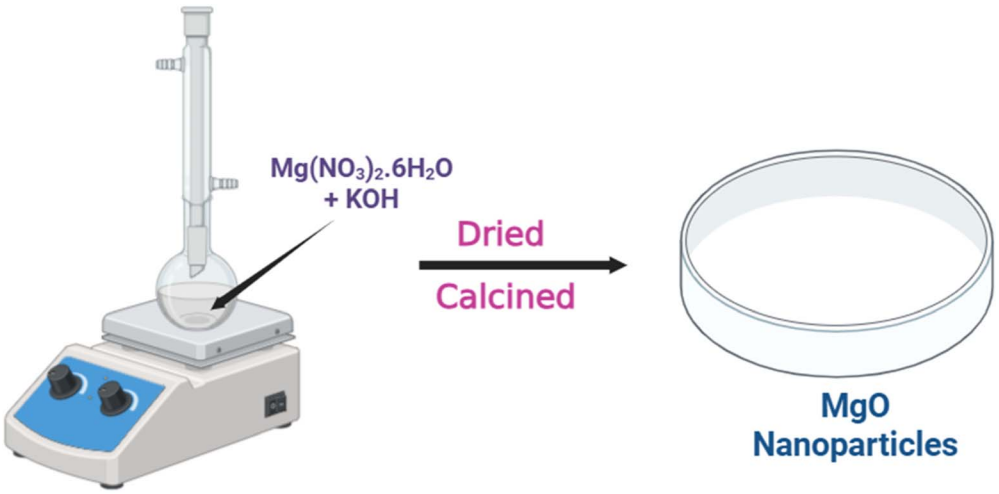

Fig. 1 Synthesis of MgONPs *via* co-precipitation method.

spectra were recorded with a confocal Raman spectroscope (Horiba LabRAM HR Evolution) using a 532 nm laser source. The electrochemical performance of the MgO electrodes was evaluated with an Admiral electrochemical workstation.

2.3 Synthesis of MgO nanoparticles (co-precipitation method)

The 0.02 M $Mg(NO_3)_2 \cdot 6H_2O$ were dispersed in deionized water. The particles were then fully dispersed using a magnetic stirrer at room temperature. After that, 1 M KOH solution was added in deionized water, and it was added to the above-prepared solution.[52,53] Following 8 hours of reaction at a temperature of 120 °C, a white precipitate of magnesium hydroxide developed in the beaker as shown in eqn (1).

$$Mg(NO_3)_2 + 2KOH \rightarrow Mg(OH)_2 + 2KNO_3 \quad (1)$$

The precipitate was subjected to filtration and several washes in methanol to get rid of any ionic impurities; after that, it was dried in air (eqn (2)).

$$Mg(OH)_2 \rightarrow MgO + H_2O \quad (2)$$

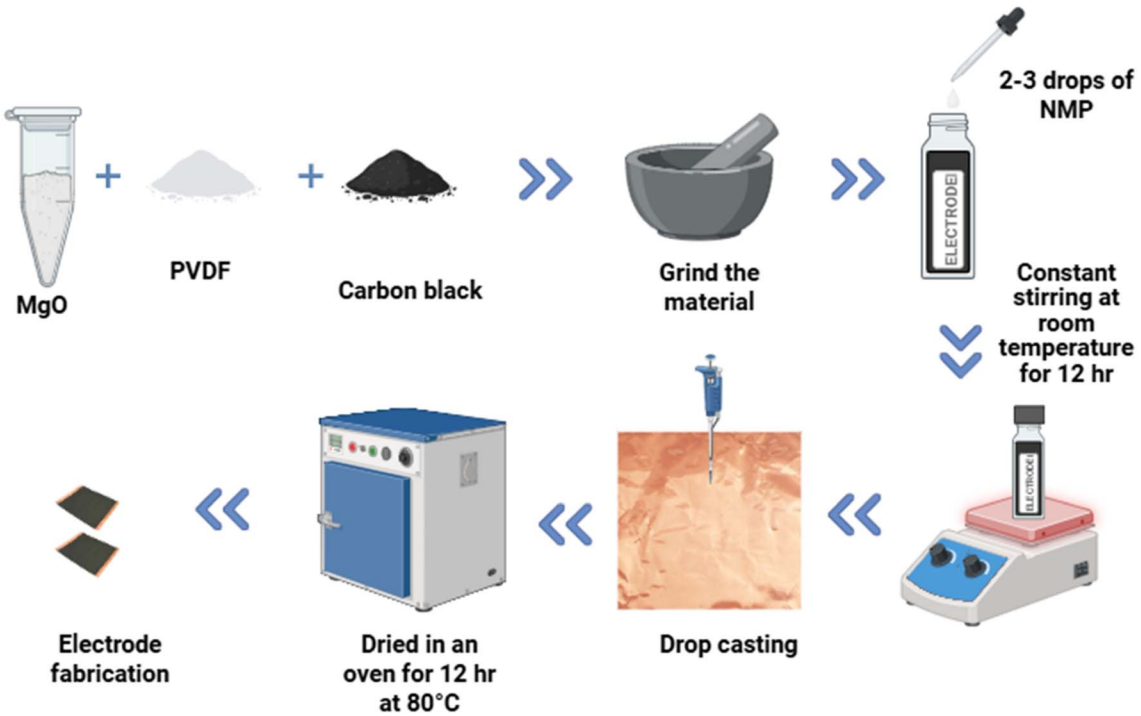

Fig. 2 Schematic illustration of the fabrication of MgONPs electrodes.

The collected precipitate was dried overnight using an oven. Finally, calcination at 500 °C for 3 hours is performed to obtain the MgO product (Fig. 1).

2.4 Electrode fabrication

2.4.1 Three electrode fabrication. Working electrodes composed of MgONPs were used in electrochemical experiments, prepared using a slurry coating procedure. To fabricate the slurry, the active material was thoroughly mixed with carbon black and PVDF in a weight ratio of 8 : 1 : 1, using *N*-methyl-2-pyrrolidone (NMP) as the solvent. The resulting slurry was uniformly coated onto copper foil, which served as the current collector, and vacuum-dried at 80 °C for 12 hours. The prepared material covered a surface area of 1 × 1 cm^2. An electrolyte solution was prepared by dissolving 2 M KOH in deionized water (Fig. 2). The working electrode was composed of the prepared material, with a platinum wire as the counter electrode and a saturated calomel electrode (SCE) as the reference electrode.[54–56] The final electrode mass loaded on current collector was 3 mg.

3. Experimental results and discussion

3.1 X-ray diffraction

The XRD analysis of MgONPs confirms their highly crystalline nature with a face-centered cubic (FCC) structure, matching the JCPDS card no. 89-7746 as shown in Fig. 3.[57] The diffraction peaks at $2\theta = 37°$, 43°, 62°, 74°, and 78° correspond to the (111), (200), (220), (311), and (222) planes, respectively. The sharp and intense peak at 43° (200 plane) is the most prominent, indicating dominant crystal growth along this orientation and confirming the material's phase purity and structural integrity. Other peaks, such as those at 37° (111 plane) and 62° (220 plane), further support the FCC structure, while peaks at 74° (311 plane) and 78° (222 plane) signify higher-order reflections, confirming three-dimensional crystallographic alignment.

The phase formation and purity of prepared nanoparticles was analysed by PXRD analysis and its average crystal size for nanoparticles was measured using Scherrer's eqn (3) with help of full width at half-maximum (FWHM) evidence.[58]

$$D = \frac{K\lambda}{\beta \cos \theta} \quad (3)$$

where K = constant, which is equal to 0.94, λ = wavelength of CuKα radiation (1.5406 Å), β = FWHM, and θ = Bragg's angle.

The crystallite size of MgO nanoparticles was calculated using Scherrer's equation, yielding an average size of approximately 8 nm. Minor unlabelled peaks with low intensity are attributed to adsorbed moisture, surface hydroxides, or residual precursors, but these do not correspond to any known crystalline impurities and do not affect the nanoparticles' crystallinity or electrochemical performance. Additionally, DFT-optimized Mg–O bond lengths (1.95–1.99 Å) align well with the experimental lattice parameters, providing further evidence of the structural integrity and phase purity of the synthesized MgONPs. This comprehensive analysis highlights the high quality, purity, and crystallinity of the nanoparticles, making them suitable for advanced material applications.

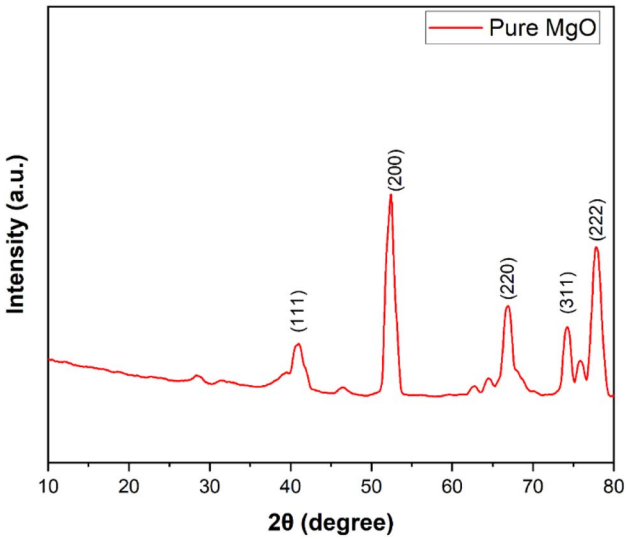

Fig. 3 XRD analysis of MgONPs electrode.

3.2 Field-emission scanning electron microscopy (FESEM)

The SEM analysis of the MgONPs reveals a non-uniform distribution of particles in an aggregated form, exhibiting a rough and porous surface (Fig. 4a). The spherical particles appear irregularly shaped with sharp edges, indicating a crystalline nature consistent with synthesis *via* chemical or combustion methods.[59,60] This morphology enhances the surface area and is advantageous for applications requiring efficient ion or reactant diffusion, such as catalysis, sensing, and energy storage. The aggregation is likely due to interparticle interactions during the synthesis process.

The EDX analysis confirms the chemical composition of the synthesized MgONPs, with prominent peaks for magnesium (Mg), oxygen (O), and silicon (Si), along with a minor contribution from potassium (K). Oxygen, contributing a weight percentage of 44.4% and an atomic percentage of 56.6%, confirms its role in the Mg–O lattice structure. Magnesium, with a weight percentage of 29.7% and an atomic percentage of 24.9%, validates the formation of MgO nanoparticles. Silicon, observed at 23.9% by weight and 17.4% by atomic percentage, may result from substrate contamination or adsorption during synthesis, though it does not disrupt the primary MgO crystalline structure. Potassium, present in trace amounts (2% by weight and 1.1% by atomic percentage), likely originates from synthesis additives or residual precursors, with negligible impact on the material's properties (Fig. 4b). Overall, the combined SEM and EDX analysis confirms the successful synthesis of highly pure MgO nanoparticles with a porous and aggregated morphology.

3.3 FTIR analysis

The FTIR spectrum of MgO, as shown in Fig. 5, reveals several characteristic peaks that confirm the structural and surface

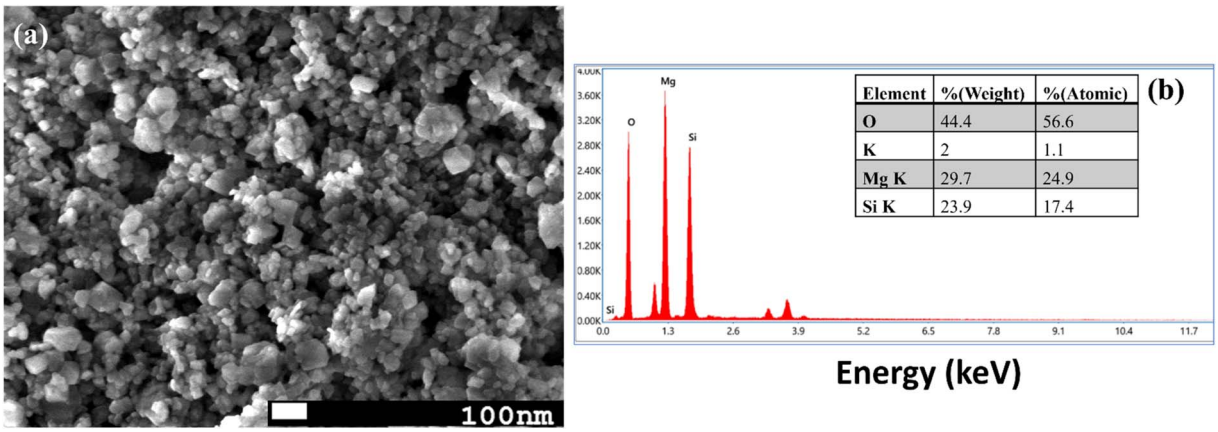

Element	%(Weight)	%(Atomic)
O	44.4	56.6
K	2	1.1
Mg K	29.7	24.9
Si K	23.9	17.4

Fig. 4 MgONPs electrode (a) FESEM; (b) EDX profile with elemental composition.

properties of the material. The broad peak at 3691 cm^{-1} is attributed to the O–H stretching vibration, indicating the presence of surface-adsorbed hydroxyl groups, likely introduced during synthesis or from ambient moisture.[61,62] This suggests enhanced surface reactivity, which is advantageous for catalytic and adsorption applications. The peak at 1650 cm^{-1} corresponds to the bending mode of molecular water (H–O–H), signifying minor moisture retention on the MgO surface. While not structurally significant, this retained moisture reflects partial hydration, which could influence the surface interactions in certain environments.

The peak observed at 1365 cm^{-1} is assigned to the C–O stretching vibration, indicative of oxygen-containing functional groups, likely arising from interactions with organic or atmospheric species during synthesis or storage. Such groups can enhance the material's compatibility with organic systems. The strong peak at 820 cm^{-1} represents the Mg–O stretching vibration, confirming the presence of magnesium oxide and validating the successful synthesis of MgO with its characteristic lattice structure.[63] This band underscores the ionic nature of the Mg–O bond, providing insight into the material's structural and electronic properties.

Additionally, theoretical insights from Mulliken charge distribution obtained *via* DFT analysis align with the FTIR results, highlighting polarized electron density between Mg and O atoms. This polarization supports the ionic character inferred from the Mg–O stretching band observed at 820 cm^{-1}, providing further evidence of the structural integrity of MgO. Together, the FTIR and DFT results confirm the presence of hydroxyl groups, minor moisture, functional groups, and Mg–O bonds, establishing the material's chemical and structural attributes, which are critical for its performance in various applications.

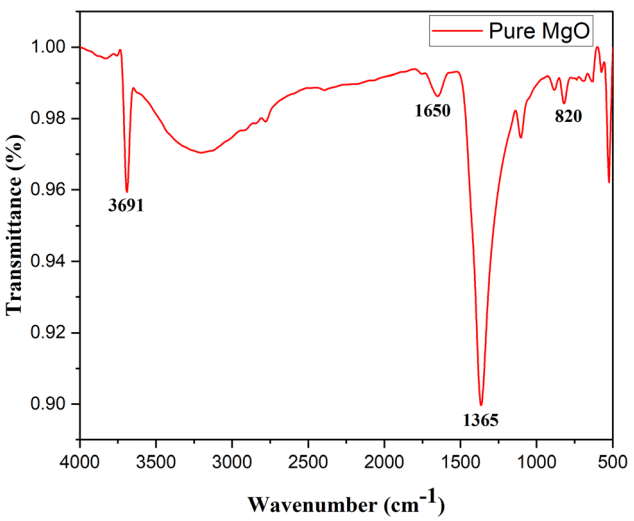

Fig. 5 FTIR analysis of MgONPs electrode.

3.4 UV-visible spectroscopy studies

The optical properties of MgONPs were analyzed using UV-Vis spectroscopy (Fig. 6a) and Tauc plot (Fig. 6b) to determine the optical band gap. The UV-Vis absorption spectrum, exhibits a significant absorption peak at approximately 300 nm, indicative of the band-to-band electronic transition from the valence band to the conduction band. This sharp peak confirms the successful synthesis of nanoscale MgONPs and reflects their characteristic optical behavior. The absorbance value of 0.0714 at this wavelength, recorded at room temperature, is consistent with the expected optical response for MgONPs. The observed peak at 300 nm also corresponds to the red color of the material, further confirming the formation of magnesium oxide nanoparticles with well-defined optical properties.

To determine the band gap energy (E_g), Tauc plot was employed using the eqn (4)

$$(\alpha h\nu) = A(h\nu - E_g)^r \quad (4)$$

where, α = optical absorption coefficient, $h\nu$ = photon energy, E_g is the direct band gap, A = constant, and $r = 1/2$ for direct allowed transitions.

Fig. 6b illustrates the Tauc plot, where the linear portion of the curve is extrapolated to intercept the photon energy $h\nu$ axis at $(\alpha h\nu)^2 = 0$.[64] The calculated optical band gap energy of

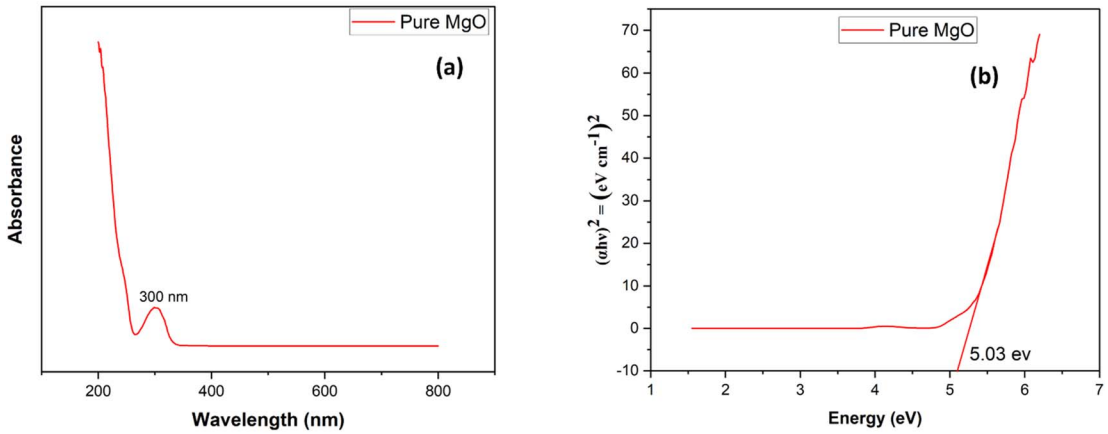

Fig. 6 MgONPs electrode (a) UV-Vis spectrum (b) band gap using the Tauc plot.

MgONPs was found to be 5.03 eV. This experimentally determined band gap aligns closely with the DFT-calculated.[65] HOMO–LUMO gap ($\Delta E = -6.571$ eV), considering the quantum confinement effects inherent to nanoparticles. Such agreement highlights the structural and electronic consistency of the synthesized MgONPs.

3.5 Raman analysis

Raman spectroscopy was utilized to investigate the vibrational properties of pure MgO, and the resulting spectrum reveals distinct peaks at 1043 cm^{-1}, 1354 cm^{-1}, and 3641 cm^{-1}, as shown in Fig. 7. These peaks, absent in bulk MgO due to its centrosymmetric cubic structure and associated Raman inactivity, signify the influence of structural defects and surface interactions in the synthesized nanomaterial.

The peak observed at 1043 cm^{-1} is attributed to defect-induced phonon modes. These modes are likely associated with oxygen vacancies, a common defect in nanostructured or polycrystalline MgO. Oxygen vacancies are known to create localized vibrational states, which contribute to the enhancement of Raman activity in such materials. Similarly, the peak at 1354 cm^{-1} corresponds to another defect-induced vibrational mode, which may arise from grain boundaries and surface irregularities. Grain boundaries in nanostructures act as scattering centers, further enhancing the vibrational modes detected in Raman spectroscopy. Together, these peaks highlight the presence of nanoscale structural imperfections, which play a critical role in modifying the material's electronic and vibrational properties. The high-frequency peak at 3641 cm^{-1} is associated with the stretching vibrations of adsorbed hydroxyl (–OH) groups. The presence of this peak suggests surface interactions with atmospheric moisture during or after the synthesis process.[66,67] These hydroxyl groups are indicative of surface passivation and could impact the material's surface chemistry and electrochemical behavior, especially in energy storage and catalytic applications.

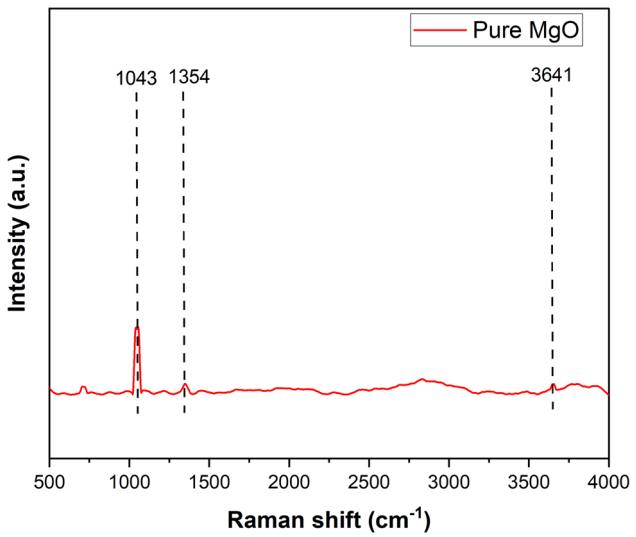

Fig. 7 Raman spectra of MgONPs electrode.

The Raman spectrum, with its prominent defect-induced peaks and evidence of surface modifications, confirms the presence of structural imperfections in MgO. These imperfections, while deviating from the ideal crystalline structure, may offer functional advantages in specific applications. For instance, oxygen vacancies and grain boundaries can enhance ion mobility and charge storage capacity, making the material suitable for electrochemical devices.[68] Further refinement of synthesis methods, such as controlled atmosphere processing or post-synthesis annealing, could optimize the defect concentration and crystallinity of MgO, tailoring it for targeted functional applications.

4. Computational results and discussion

4.1 Quantum chemical calculations

4.1.1 Density functional theory (DFT) study. DFT study to investigate the structural and electronic structure of pure MgONPs. The computational experiment was performed to optimize the pure MgONPs as a model system in its ground

state energy. The optimization procedure was followed by the frequency calculations *via* the DFT approach using the B3LYP functional coupled with 6-31G basis set for the O and Mg atoms in the gas and solvent (water) phases.[69] The energies of the highest occupied molecular orbital (HOMO) and lowest unoccupied molecular orbitals (LUMO) acquired from the Frontier molecular orbitals (FMOs) were computed. The difference in energy between the two FMOs, HOMO and LUMO is known as the HLEG (ΔE). The ΔE value is utilized to characterize the chemical behaviour of the systems. Like, in terms of the chemical nature of any molecule, more stability of a system implies that it is consisting of a higher E_{gap} value (larger reactivity). Due to the high reactivity of the molecules, interactions between MgO are facilitated by a less gap of $\Delta E = E_{LUMO} - E_{HOMO}$. A large HLEG value means that the system consists of less reactivity where a small HLEG value refers about its more reactivity of the system.[70–74]

The equilibrium geometry of a molecule is determined by calculations of its energy and frequency calculations. When energy of any molecule is minimal, it is in its most stable configuration, known as its equilibrium/optimized. The optimization (equilibrium/minimum energy) configuration of the MgONPs can be viewed in Fig. S1 (a) of the ESI† with appropriate atomic labelling along with some selected structural parameters like bond lengths for the MgONPs. The equilibrium (optimized) structure of the MgONPs (MgO cluster at the top), it shows that the calculated Mg–O bond lengths (see at the top right terminal) were calculated to be 1.951 Å in the gas phase while 1.985 Å in the solvent phase. The analysed bond lengths of the central Mg–O bonds for the pure MgO cluster are 1.960 Å (in the gas phase) and 1.988 Å in the solvent phase whereas 2.06 Å in the gas phase and 2.059 Å in the solvent phase (water) for the Mg–O bonds lying at the left-central fragment. Similarly, the bond distances of another Mg–O bond (located at the central-bottom) for the undoped MgONPs are found to be 1.973 Å and 1.99 Å in the gas and solvent (water) phases, correspondingly. Such findings suggest that the MgONP could help in designing the smart doped-MgONPs for energy storage applications due to its the preferable interaction showing the desirable binding between the Mg/O atoms of the MgO cluster or other prototypes.

The DFT results reveal strong electronic interactions between Mg and O atoms, supported by a low HOMO–LUMO gap ($\Delta E = -6.571$ eV), indicating high molecular reactivity and effective charge transfer (Fig. S1 (b) of the ESI†). The system also exhibits high softness (−0.304 eV), low hardness (−3.285 eV), and a notable dipole moment (7.3 D), suggesting enhanced polarity and favorable electrostatic interactions. An electronegativity value of 7.353 further supports the material's tendency to attract electrons, contributing to its electrochemical activity. The computed electrophilicity (−8.229 eV) indicates strong electron-accepting ability. These quantum chemical descriptors (summarized in Table S1 of the ESI†) align well with the experimental findings, particularly the observed high specific capacitance and coulombic efficiency. Mulliken charge analysis (Fig. S2 (b) of the ESI†) confirms balanced charge distribution, validating the structural stability and reactivity of MgONPs. The close agreement between DFT predictions and electrochemical performance supports the reliability of MgONPs as a high-performance supercapacitor material.[75,76]

Fig. S2 (a) of the ESI† shows the cubic lattice arrangement, where Mg (green) and O (red) atoms form a 3D network with characteristic ionic bonding. Fig. S2 (b) of the ESI† presents a radar chart of Mulliken charges, highlighting the charge distribution across individual atoms using a red-to-green gradient to indicate relative negativity or positivity. These visualizations collectively provide insight into the structural symmetry and electronic environment of MgO, supporting its stability and electrochemical functionality.

5. Electrochemical performance results and discussion

The charge storage characteristics of the multilayered MgONPs electrodes for supercapacitor applications. Individual electrode parameters were investigated using a 2 M KOH solution to gain a better understanding of the charge storage characteristics of three electrode systems.

5.1 Cyclic voltammetry (CV) analysis

At different sweep rates (10 to 200 mV s^{-1}), the individual CV curves of MgONPs electrodes were measured, as shown in Fig. S3 of the ESI.† Even at a higher sweep rate of 100 mV s^{-1}, the CV profile maintains well-defined redox plateaus, demonstrating the electrode's high-rate capabilities. Fig. 8a presents the CV profiles of MgO electrodes recorded over a potential window of 0–1.0 V at varying scan rates ranging from 10 to 200 mV s^{-1}. The CV curves exhibited a quasi-rectangular shape with slight distortion, characteristic of dominant electric double-layer capacitance (EDLC) behavior with minor pseudocapacitive contributions. Importantly, even at a higher sweep rate of 100 mV s^{-1}, the CV profiles maintained well-defined redox plateaus, highlighting the high-rate capabilities of the MgONPs electrodes. This retention of CV shape at elevated scan rates suggests good electrochemical reversibility and efficient ion transport within the electrode material.

As the scan rate increases, a corresponding enhancement in peak current is observed, indicating improved electron transfer kinetics. However, a reduction in the enclosed CV area was noted at higher scan rates, attributed to diffusion limitations that prevent complete access of electrolyte ions to the internal active surface. Such a trend is common in nanostructured porous materials and underscores the role of diffusion kinetics in capacitive performance.

Fig. 8b and Table 2 presents the variation in specific capacitance (C_s) as a function of scan rate. The C_s was calculated from CV data using the eqn (5):

$$C_s = \frac{A}{m \times \Delta V \times \nu} \quad (5)$$

where C_s is in F g^{-1}, and A, m, ΔV, and ν represent the integrated area of the CV curve, deposited mass, potential window, and scan rate, respectively.

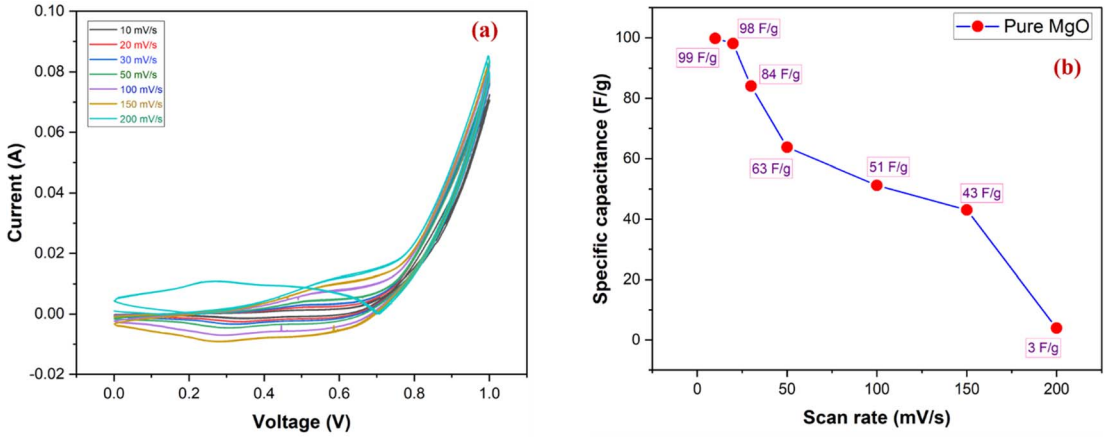

Fig. 8 (a) Different sweep rates of CV for MgONPs electrodes, (b) the variation of the specific capacitance with various scan rates of MgONPs electrode.

The MgONPs electrode demonstrated a maximum specific capacitance of 99 F g^{-1} at a scan rate of 10 mV s^{-1}. However, as the scan rate increased to 200 mV s^{-1}, the specific capacitance significantly dropped to 3 F g^{-1}. This pronounced decline can be attributed to insufficient time for electrolyte ions to diffuse into the internal porous structure at higher scan rates, thereby reducing effective charge storage. The trend highlights the influence of ion diffusion kinetics on capacitive performance.

Despite the reduction in specific capacitance at higher scan rates, the high capacitance at low scan rates validates the potential of MgONPs as a promising electrode material for supercapacitors. The observed performance is particularly suitable for low-power or trickle-charge applications. Further structural optimization, such as doping, nano structuring, or forming composites, could enhance the material's rate capability by mitigating diffusion limitations and maximizing active surface area accessibility.

5.2 Galvanostatic charge–discharge (GCD) analysis

The GCD analyses were obtained by varying the current rates from 0.1 to 3.3 A g^{-1}, as shown in Fig. S4 of the ESI.† The charge–discharge curves exhibit a linear increase in their applied current densities, with no observed IR drop in the charge storage curves. The GCD curves exhibit a quasi-linear and symmetrical triangular shape, characteristic of ideal capacitive behavior (Fig. 9a). Notably, the absence of prominent plateaus confirms the predominance of electric double-layer capacitance (EDLC) behavior, with minimal contribution from faradaic redox processes.

Table 2 Specific Capacitance of the MgONPs electrode at different scan rates

Scan rate (mV s^{-1})	Specific capacitance (F g^{-1})
10	99
20	98
30	84
50	63
100	51
150	43
200	3

The discharge duration is inversely related to the applied current density, with longer discharge times observed at lower currents (*e.g.*, 0.1 A g^{-1}) and progressively shorter durations at higher rates (up to 3.3 A g^{-1}). This behavior reflects the expected increase in ohmic resistance and decreased ionic diffusion efficiency at elevated current densities.

The specific capacitance (C_s) values were extracted from the discharge portions of the GCD curves using the standard eqn (6):

$$C_s = \frac{I \times \Delta t}{m \times \Delta V} \quad (6)$$

where C_s = specific capacitance (F g^{-1}), I = current applied (A), Δt = discharge time (s), ΔV = potential window (V) and m = mass of electroactive material (g).

The resulting capacitance values are summarized in Fig. 9b, which clearly shows a decreasing trend in specific capacitance with increasing current density. A maximum capacitance of 28 F g^{-1} was obtained at 0.1 A g^{-1}, which gradually diminished to 5 F g^{-1} at 10 A g^{-1}. The long-term cycling performance of the MgO-based electrode was evaluated at a current density of 0.2 A g^{-1} for over 800 consecutive charge–discharge cycles, as shown in Fig. 9c. The electrode exhibited excellent cycling stability, with capacity retention remaining close to 99% after the full test duration. This minimal degradation highlights the structural robustness and high electrochemical reversibility of the MgONPs. The steady performance over prolonged cycling suggests strong interfacial contact between the active material and electrolyte, with minimal loss of active sites or mechanical breakdown. Such stability is essential for practical supercapacitor applications, confirming the suitability of MgO as a promising electrode material for energy storage systems.

This performance drop is commonly attributed to the inability of electrolyte ions to fully access the internal active sites of MgO under rapid charge–discharge conditions. The limited ion diffusion and increased polarization losses at high

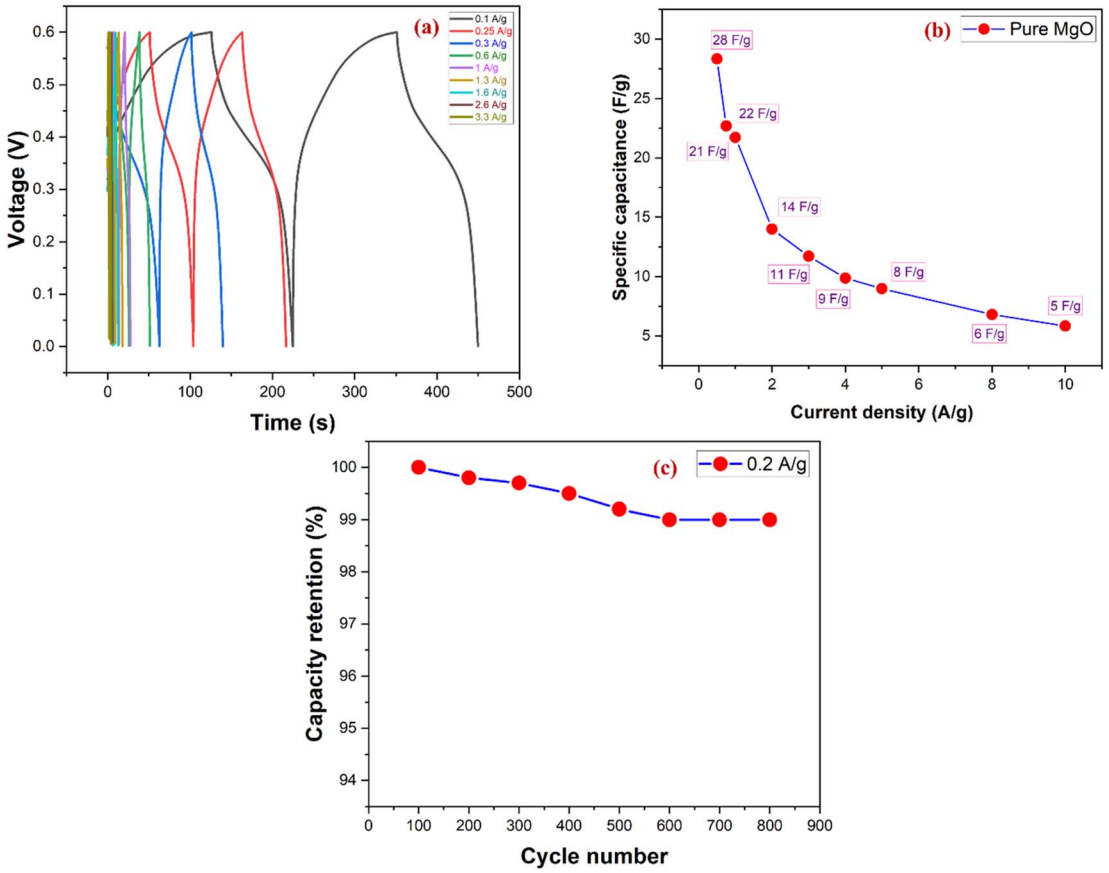

Fig. 9 (a) Different current density of GCD for MgONPs electrodes, (b) the variation of specific capacitance with various current densities of MgONPs electrodes, (c) cyclic performance at 0.2 A g^{-1} (800 cycles) with capacity retention.

current densities restrict the full utilization of electrochemically active surface area. Nevertheless, the relatively stable shape of the GCD profiles and the retention of capacitance at higher currents reflect the structural robustness and electrical integrity of the MgO electrode. These findings underscore the promise of pure MgO for supercapacitor applications, particularly where moderate energy storage and high durability are required. Future work may focus on enhancing rate performance *via* compositional tuning (*e.g.*, carbon composites or heteroatom doping) or morphological engineering (*e.g.*, mesoporous structuring).

The high specific capacitance (99 F g^{-1}) and excellent rate capability are supported by DFT-derived descriptors, including high dipole moment (7.3 *D*), low hardness (−3.285 eV), and significant softness (−0.304 eV^{-1}), indicating favorable charge redistribution and electrochemical activity.

5.3 Electrochemical impedance spectroscopy (EIS), Ragone, and Bode plot analysis

EIS was performed to evaluate the charge transport dynamics and resistive characteristics of the pure MgO electrode, as illustrated in Fig. 10a. The Nyquist plot exhibits a semicircular profile in the high-frequency region, representing the charge transfer resistance (R_{ct}), and a linear tail in the low-frequency region, indicative of diffusion-controlled processes. The R_{ct} derived from the diameter of the semicircle, is approximately 10 Ω, suggesting moderate resistance at the electrode–electrolyte interface during faradaic reactions. The equivalent series resistance (R_s), measured as the intercept on the real axis, is approximately 2.5 Ω, signifying minimal ohmic losses and excellent ionic conductivity. The linear Warburg region at low frequencies highlights ion diffusion within the porous MgO structure. The fitting curve closely aligns with the experimental data, validating the equivalent circuit model used for analysis. These impedance parameters confirm that the MgO electrode maintains both structural integrity and electrochemical stability under operational conditions, supporting its applicability as a cathodic material in supercapacitor systems.

The Ragone plot (Fig. 10b) evaluates the capacitive performance in terms of energy and power density. At a low power density of 49.4 W kg^{-1}, the MgO electrode delivers a maximum energy density of 1.38 Wh kg^{-1}, which decreases to 0.27 Wh kg^{-1} as the power density increases to 966.9 W kg^{-1} due to diffusion limitations. This trend underscores the MgO electrode's suitability for moderate-power applications, balancing energy and power requirements. Table S2 of the ESI† gives the energy and power density for 3 electrode method.

Energy density (E_d) and power density (P_d) values of MgONPs electrode were calculated by using eqn (7) and (8) respectively.

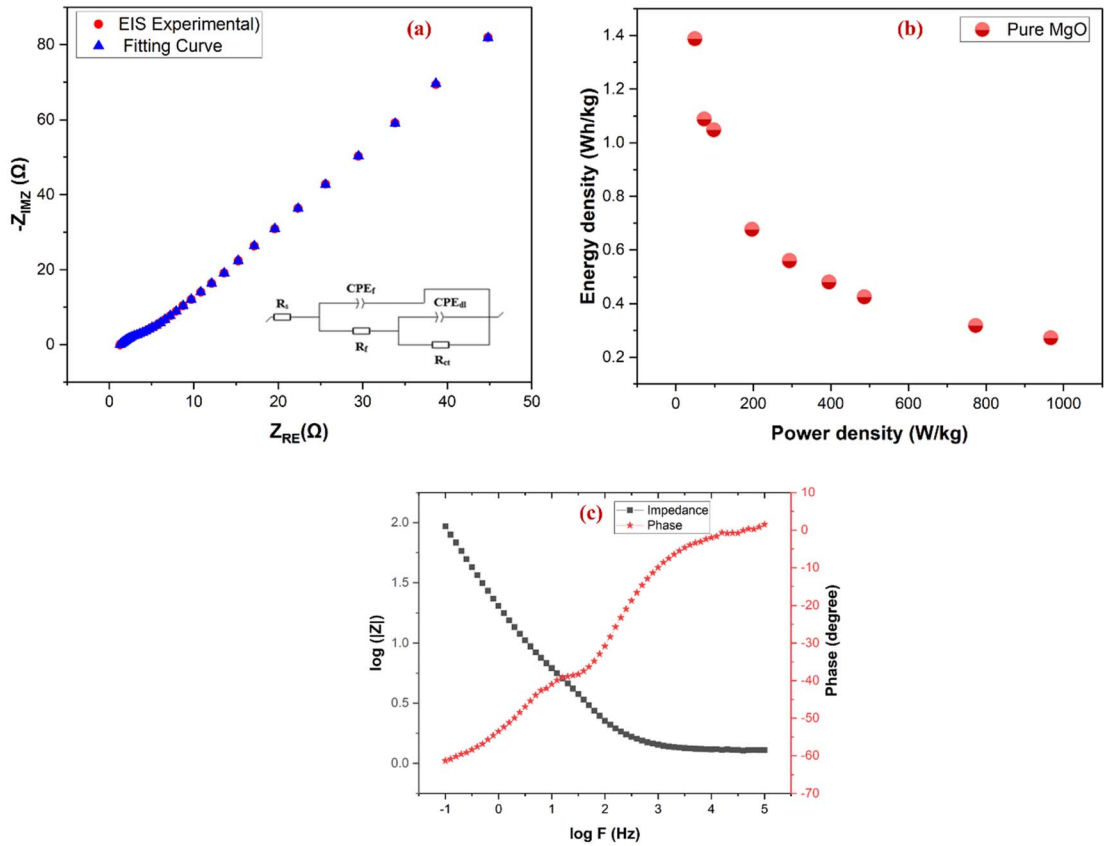

Fig. 10 (a) EIS, (b) Ragone plot, and (c) Bode plot for MgONPs electrode.

$$\text{Energy density}\left(\text{Wh kg}^{-1}\right) = \frac{1}{2}C_s v^2 \quad (7)$$

where, C_s is the specific capacitance value from GCD data, v is the maximum operational potential window.

$$\text{Power density}\left(\text{W kg}^{-1}\right) = \frac{E}{t_d} \quad (8)$$

where, E is the energy density, t_d is the discharge time.

The Bode plot (Fig. 10c) provides further insights into the frequency-dependent behavior of the electrode. The impedance magnitude ($|Z|$) decreases with increasing frequency, indicating a transition from resistive to capacitive behavior. The phase angle shifts from approximately $-65°$ at low frequencies, reflecting capacitive dominance, to 0° at high frequencies, highlighting resistive contributions. The characteristic frequency (f_0), at which the phase angle is $-45°$, corresponds to the electrode's time constant ($\tau_0 = 1/f_0$), providing critical information about its rate capability and responsiveness. Together, these results confirm the MgO electrode's structural integrity, efficient charge transport, and promising potential for supercapacitor applications.

The collective evaluation of the EIS analysis, Ragone plot, and Bode response underscores the versatility of the pure MgO electrode. It demonstrates a low internal resistance, commendable rate capability, and a balanced trade-off between energy and power densities. While pure MgO may not achieve the energy densities characteristic of pseudocapacitive materials, its competitive performance in EDLC-type applications, coupled with good electrochemical stability, positions it as a promising candidate for moderate-power supercapacitors. These findings suggest that pure MgO can serve as a robust foundation for hybridization with high-capacitance materials, thereby enhancing its overall functionality. Furthermore, the preliminary outcomes of newly designed doped-MgONPs highlight intriguing properties, paving the way for future investigations. Upcoming studies will extend this work by explicitly addressing the experimental and theoretical outcomes of these novel MgONP-based materials, emphasizing their unique characteristics and potential applications.

6. Conclusion

This work presents a comprehensive investigation of MgO nanoparticles as high-performance electrode materials for supercapacitors by combining experimental evaluation with first-principles DFT simulations. Experimentally, MgONPs demonstrated excellent electrochemical performance, with a high specific capacitance (99 F g^{-1} at 10 mV s^{-1}), good rate stability, and low internal resistance, highlighting their suitability for energy storage applications. Theoretical insights from DFT calculations revealed a low HOMO–LUMO energy gap and favorable electronic properties such as high dipole moment

and significant molecular softness, which corroborate the high charge mobility and capacitance observed experimentally. Furthermore, the consistency between calculated Mg–O bond lengths and experimental XRD data validated the structural fidelity of the synthesized nanoparticles. The Mulliken charge distribution confirmed balanced electron density, supporting stable charge storage and transfer behavior. This dual approach not only elucidates the fundamental electrochemical mechanisms at play but also validates the potential of MgONPs as efficient, stable, and sustainable materials for supercapacitor technology. Future work will explore doped and hybridized MgO nanostructures to further enhance energy and power density.

Data availability

The data will be available on the genuine request.

Conflicts of interest

The authors declare no conflict of interest.

Acknowledgements

The authors are grateful for the assistance of Central Analytical Facility (CAF) and Sophisticated Analytical Instrument Facility (SAIF) for the high throughput analysis *i.e.* FTIR, SEM, XRD, UV-Vis, and RAMAN analysis at Manipal University Jaipur. SKP is thankful to MANIT Bhopal for facilitating computational facilities.

References

1 S. Vinoth, H. T. Das, M. Govindasamy, S.-F. Wang, N. S. Alkadhi and M. Ouladsmane, *J. Alloys Compd.*, 2021, **877**, 160192.
2 T. M. Gür, *Energy Environ. Sci.*, 2018, **11**, 3055.
3 M. Y. Worku, *Sustainability*, 2022, **14**, 5985.
4 M. Rezaeimozafar, R. F. Monaghan, E. Barrett and M. Duffy, *Renewable Sustainable Energy Rev.*, 2022, **164**, 112573.
5 X. Li, L. Zhang, H. Chai, Y. Zhang, R. Wang, M. Xie, Y. Xu, J. Chen and Y. Jiao, *J. Colloid Interface Sci.*, 2023, **632**, 186–195.
6 S. Sridhar and S. R. Salkuti, *Smart Cities*, 2022, **5**, 668–699.
7 A. Patel, S. K. Patel, R. Singh and R. Patel, *Discover Nano*, 2024, **19**, 188.
8 J. M. Baptista, J. S. Sagu, U. W. Kg and K. Lobato, *Chem. Eng. J.*, 2019, **374**, 1153–1179.
9 J. Cheng, B. Mi, Q. Wang, H. Wang, T. Zhou, Y. Li, H. Hou and Y. Zhu, *Chem. Eng. J.*, 2025, 161242.
10 J. Zhang, M. Gu and X. Chen, *Micro Nano Eng.*, 2023, **21**, 100229.
11 P. Sharma and T. Bhatti, *Energy Convers. Manage.*, 2010, **51**, 2901–2912.
12 B. Conway, *Electrochemical Supercapacitors*, 1999, p. 698.
13 M. Goyal, S. N. Agarwal, K. Singh and N. Bhatnagar, *J. Appl. Polym. Sci.*, 2023, **140**, e53830.
14 M. Goyal and N. Bhatnagar, *J. Appl. Polym. Sci.*, 2025, e57154.
15 M. Goyal, K. Singh and N. Bhatnagar, *Prog. Org. Coat.*, 2024, **187**, 108083.
16 M. Goyal, M. Chawla, K. Singh and N. Bhatnagar, *J. Appl. Polym. Sci.*, 2025, e57429.
17 S. A. Kumar, S. Sahoo, G. K. Laxminarayana and C. S. Rout, *Small*, 2024, **20**, 2402087.
18 M. Geerthana, S. Prabhu and R. Ramesh, *J. Energy Storage*, 2022, **47**, 103529.
19 R. Vicentini, R. Beraldo, J. P. Aguiar, F. E. Oliveira, F. C. Rufino, D. R. G. Larrude, L. M. Da Silva and H. Zanin, *J. Energy Storage*, 2021, **44**, 103371.
20 S. Nagarani, G. Sasikala, M. Yuvaraj, R. D. Kumar, S. Balachandran and M. Kumar, *J. Energy Storage*, 2022, **52**, 104969.
21 P. Sengodan, R. Govindan, G. Arumugam, B. Chettiannan, M. Navaneethan, M. R. Pallavolu, M. Hussien, M. Selvaraj and R. Rajendran, *J. Energy Storage*, 2022, **50**, 104625.
22 M. Moharramnejad, A. Ehsani, R. E. Malekshah, M. Shahi, H. H. Qezelje, M. Nekoeifard, E. Azarash and H. Parsimehr, *J. Mater. Sci.: Mater. Electron.*, 2023, **34**, 499.
23 H. Kuzhandaivel, K. Paramasivam, S. Manickam and K. S. Nallathambi, *J. Appl. Electrochem.*, 2023, **53**, 1869–1886.
24 H. Cao, Y. Pan, C. Shi, L. Guo, J. Yang and Y. Wang, *Diamond Relat. Mater.*, 2022, **122**, 108806.
25 R. Patil, A. Yadav, R. Gurav, A. Patil, S. Mali, S. Pawar and S. Patil, *Bull. Mater. Sci.*, 2024, **47**, 193.
26 W. Han, M. Zhong, H. Ju, D. Chen, L. Yuan, X. Liu and C. Wang, *ChemElectroChem*, 2022, **9**, e202200122.
27 M. Goyal, K. Singh and N. Bhatnagar, *ChemistrySelect*, 2024, **9**, e202400543.
28 S. Nagaoka, K. Hamasaki, T. Yamashita and T. Komata, *Jpn. J. Appl. Phys.*, 1989, **28**, 1367.
29 S. Shukla, G. Parashar, A. Mishra, P. Misra, B. Yadav, R. Shukla, L. Bali and G. Dubey, *Sens. Actuators, B*, 2004, **98**, 5–11.
30 P. Yang and C. M. Lieber, *Science*, 1996, **273**, 1836–1840.
31 M. Mylarappa, N. Raghavendra, B. Surendra, K. S. Kumar and S. Kantharjau, *Appl. Surf. Sci. Adv.*, 2022, **10**, 100268.
32 D. Fischer, D. Zagorac, K. Küster and J. C. Schön, *Coatings*, 2024, **14**, 1563.
33 A. Kumar and J. Kumar, *J. Phys. Chem. Solids*, 2008, **69**, 2764–2772.
34 M. Haertelt, A. Fielicke, G. Meijer, K. Kwapien, M. Sierka and J. Sauer, *Phys. Chem. Chem. Phys.*, 2012, **14**, 2849–2856.
35 Y. Xiao, X. Zhang, C. Wang, J. Rao and Y. Zhang, *J. Magnesium Alloys*, 2024, **12**, 35–58.
36 N. Rani, S. Chahal, P. Kumar, R. Shukla and S. Singh, *AIP Conf. Proc.*, 2019, 030163.
37 P. Tamilselvi, A. Yelilarasi, M. Hema and R. Anbarasan, *Nano Bulletin*, 2013, **2**, 130106.
38 F. Mirza and H. Makwana, *J. Innov. Res. Technol.*, 2021, **8**, 436–441.
39 A. Venkatachalam and J. P. Jesuraj, *J. Chem.*, 2021, 2021.
40 A. Maurya and N. Bhatia, *Int. J. Eng. Res. Dev*, 2017, **13**, 01–06.
41 K. V. Rao and C. Sunandana, *J. Mater. Sci.*, 2008, **43**, 146–154.

42 R. Farma, M. Deraman, I. Talib, R. Omar, J. Manjunatha, M. Ishak, N. Basri and B. Dolah, *Int. J. Electrochem. Sci.*, 2013, **8**, 257–273.
43 C. P. P. Wong, C. W. Lai, K. M. Lee, J. C. Juan and S. B. Abd Hamid, *Ceram. Int.*, 2016, **42**, 13128–13135.
44 Y. Kado and Y. Soneda, *Microporous Mesoporous Mater.*, 2021, **310**, 110646.
45 A. Hroub, M. H. Aleinawi, M. Stefan, M. Mihet, A. Ciorita, F. Bakan-Misirlioglu, E. Erdem and A. M. Rostas, *J. Alloys Compd.*, 2023, **958**, 170442.
46 A. K. Verma, S. Dubey and S. K. Srivastava, *Comput. Biol. Med.*, 2023, **158**, 106863.
47 F. A. Adam, M. Ghoniem, M. Diawara, S. Rahali, B. Y. Abdulkhair, M. Elamin, M. A. B. Aissa and M. Seydou, *RSC Adv.*, 2022, **12**, 24786–24803.
48 S. H. Mehdi, R. M. Ghalib, S. Awasthi, S. F. Alshahateet, R. Hashim, O. Sulaiman and S. K. Pandey, *ChemistrySelect*, 2017, **2**, 6699–6709.
49 R. Singh, K. Singh and S. K. Pandey, *ChemistrySelect*, 2018, **3**, 13048–13056.
50 A. K. Srivastava, N. Misra and S. K. Pandey, *J. Cluster Sci.*, 2018, **29**, 57–65.
51 B. Saravanakumar, S. Muthulakshmi, G. Ravi, V. Ganesh, A. Sakunthala and R. Yuvakkumar, *Appl. Phys. A:Mater. Sci. Process.*, 2017, **123**, 1–9.
52 K. Manjunatha, B. K. Swamy, H. Madhuchandra, K. Gururaj and K. Vishnumurthy, *Sens. Int.*, 2021, **2**, 100127.
53 R. Taourati, M. Khaddor, A. Laghzal and A. El Kasmi, *Sci. Afr.*, 2020, **8**, e00305.
54 B. Subramanya and D. K. Bhat, *J. Power Sources*, 2015, **275**, 90–98.
55 M. K. Sahoo, P. Gogoi, G. Rajeshkhanna, S. V. Chilukuri and G. R. Rao, *Appl. Surf. Sci.*, 2017, **418**, 40–48.
56 I. M. De la Fuente Salas, Y. Sudhakar and M. Selvakumar, *Appl. Surf. Sci.*, 2014, **296**, 195–203.
57 S. Sasaki, K. Fujino and Y. Takéuchi, *Proc. Jpn. Acad., Ser. B*, 1979, **55**, 43–48.
58 M. Rezaei, M. Khajenoori and B. Nematollahi, *Mater. Res. Bull.*, 2011, **46**, 1632–1637.
59 B. Clavier, T. Baptiste, Z. Barbieriková, T. Hajdu, A. Guiet, F. Boucher, V. Brezová, C. Roques and G. Corbel, *Mater. Sci. Eng. C*, 2021, **123**, 111997.
60 R. Narayanan and M. A. El-Sayed in *Catalysis with Transition Metal Nanoparticles in Colloidal Solution: Nanoparticle Shape Dependence and Stability*, ACS Publications, Vol. 109, 2005, pp. 12663–12676.
61 W. A. Khaleel, S. A. Sadeq, I. A. M. Alani and M. H. M. Ahmed, *Opt Laser. Technol.*, 2019, **115**, 331–336.
62 N. Sutradhar, A. Sinhamahapatra, S. K. Pahari, P. Pal, H. C. Bajaj, I. Mukhopadhyay and A. B. Panda, *J. Phys. Chem. C*, 2011, **115**, 12308–12316.
63 R. Wahab, S. Ansari, M. A. Dar, Y. S. Kim and H. S. Shin, *Mater. Sci. Forum*, 2007, 983–986.
64 P. M. Kouotou, A. El Kasmi, L.-N. Wu, M. Waqas and Z.-Y. Tian, *J. Taiwan Inst. Chem. Eng.*, 2018, **93**, 427–435.
65 R. Al-Gaashani, S. Radiman, Y. Al-Douri, N. Tabet and A. R. Daud, *J. Alloys Compd.*, 2012, **521**, 71–76.
66 M. Dekermenjian, A. P. Ruediger and A. Merlen, *RSC Adv.*, 2023, **13**, 26683–26689.
67 K. Ishikawa, N. Fujima and H. Komura, *J. Appl. Phys.*, 1985, **57**, 973–975.
68 P. Wang, Y. Guo, D. Zhou, D. Li, L. Pang, W. Liu, J. Su, Z. Shi and S. Sun, *Adv. Funct. Mater.*, 2022, **32**, 2204155.
69 K. Saadat and H. Tavakol, *Struct. Chem.*, 2016, **27**, 739–751.
70 A. Sharma, G. R. Nishad, P. Vishwakarma and P. Jaget in *Density Functional Theory (DFT)-based Molecular Modeling*, Elsevier, 2023, pp. 115–133.
71 V. Vijayalakshmi, N. Kanagathara, J. Jan, M. Marchewka, A. Mohammad and K. Senthilkumar, *Opt. Mater.*, 2024, **147**, 114694.
72 P. Lokhande, R. U. Bhaskar, D. Kumar, S. Awasthi and S. K. Pandey, *Int. J. Hydrogen Energy*, 2024, **78**, 534–546.
73 S. K. Pandey, *ACS Omega*, 2021, **6**, 31077–31092.
74 R. K. Mudsainiyan and S. K. Pandey, *Z. Anorg. Allg. Chem.*, 2017, **643**, 1245–1252.
75 T. Mandal, A. K. Ghosh, S. R. Mishra, S. K. Pandey and V. Singh, *Nanoscale Adv.*, 2023, **5**, 4269–4285.
76 A. M. F. Costa, T. S. Silva, L. B. C. Oh and D. H. Pereira, *Monatsh. Chem*, 2021, **152**, 915–922.